Materials Today 93 (2026) 103187

Contents lists available at ScienceDirect

Materials Today

journal homepage: www.elsevier.com/locate/mattod

Putting fatigue to rest via solute-pinned boundaries

Manish Jain [a,1], Daniel Vizoso [a,1], Alejandro Hinojos [b], Alejandro Barrios [c], Kyle R. Dorman [a], Yichen Yang [d], David Adams [a], Khalid Hattar [e], Doug L. Medlin [b], Olivier Pierron [d], Rémi Dingreville [a], Brad L. Boyce [a,*]

[a] Center for Integrated Nanotechnologies, Sandia National Laboratories, Albuquerque, NM, 87123, USA
[b] Sandia National Laboratories, Livermore, 94550, CA, USA
[c] Colorado School of Mines, Golden, 80401, CO, USA
[d] Georgia Institute of Technology, Atlanta, 30332, GA, USA
[e] University of Tennessee, Knoxville, 37996, TN, USA

ARTICLE INFO

Keywords:
Fatigue
Stability
Crack initiation
Grain growth
Nanocrystalline

ABSTRACT

All metals have their limit when it comes to enduring fatigue damage. The best commercial alloys can survive 10^7 cycles at cyclic stress amplitudes up to approximately 850 MPa. Here we explore the possibility of exceeding that limit by preventing dislocation-mediated crack nucleation processes. In the current study, a model solute-stabilized nanocrystalline alloy (Pt-10 atom% Au) is shown to sustain no fatigue damage even after 10^{10} cycles at stress amplitudes above 1 GPa (corresponding to an applied maximum strain of 0.65% under fully reversed loading). To understand the origins of that remarkable fatigue resistance, atomistic simulations and electron microscopy point to the role of solute-stabilized grain boundaries which prevent the nanostructured alloy from undergoing fatigue-induced grain growth and subsequent dislocation-mediated fatigue damage. Such findings point to new pathways to suppress crack initiation in nanostructured metals, offering a possibility of future metals that are impervious to fatigue failure.

Introduction

Metal fatigue is a silent killer. This cyclic damage process is responsible for 80-90% of mechanical failures, resulting in enormous economic waste and catastrophic loss of life. To prevent these elusive failures, our airplanes and cars are overdesigned, a secondary form of waste and inefficiency. In nearly all metals, the nucleation of a fatigue crack starts with a dislocation slip process [1]; the first signs of this damage can be detected on the very first loading cycle [2]. In nanocrystalline metals with grain sizes below 100 nm, size confinement restricts dislocation slip, thereby enhancing resistance to crack nucleation [3]. But nanocrystalline metals have their own Achilles heel: they undergo fatigue-induced grain growth [4], eventually resulting in microcrystalline grains that still fail by slip. A recent report illuminates the atomic-scale process for cyclic grain growth: asymmetric "Brownian ratcheting" of grain-boundary (GB) defects called disconnections [5]. Accordingly, fatigue failure in fine-grained metals is thought to begin with disconnections undulating under cyclic loading, triggering a cascade of boundary migration, grain growth, dislocation slip, crack nucleation, and eventual failure. To stop fatigue damage at its source, the mobility of disconnections must be diminished. Miscible binary alloys provide solute atoms that attach to the local strain field of disconnections, thereby impeding their movement [6–8]. Such solute additions are already well-known to impede thermally driven grain growth via kinetic and thermodynamic means [9,10].

This study focuses on a Pt-rich alloy with Au additions, as a model material for exploring fatigue resilience through GB stabilization. This alloy system has been shown to be more resistant to thermally-induced grain growth than pure nanocrystalline Pt due to the presence of Au at GBs [11,12], and has also been shown to possess excellent wear resistance [13]. Our prior work indicated that Pt-10 atom% Au (Pt-10Au) exhibits improved fatigue resistance compared to nanocrystalline pure Pt [14]. In this study, we employ a new technique based on a silicon MEMS (microelectromechanical system) resonator device. The Si device serves as a carrier to impose fatigue strains on deposited metal films, allowing exploration of extreme fatigue resistance in the gigacycle or very high cycle fatigue (VHCF) regime (10^9 cycles and more). Complementing those experiments, atomistic fatigue simulations elucidate the fatigue-driven grain-growth process and confirm the role of solute additions.

* Corresponding author.
E-mail address: blboyce@sandia.gov (B.L. Boyce).
[1] These authors contributed equally to this work.

https://doi.org/10.1016/j.mattod.2026.103187
Received 25 July 2025; Received in revised form 31 October 2025; Accepted 12 January 2026

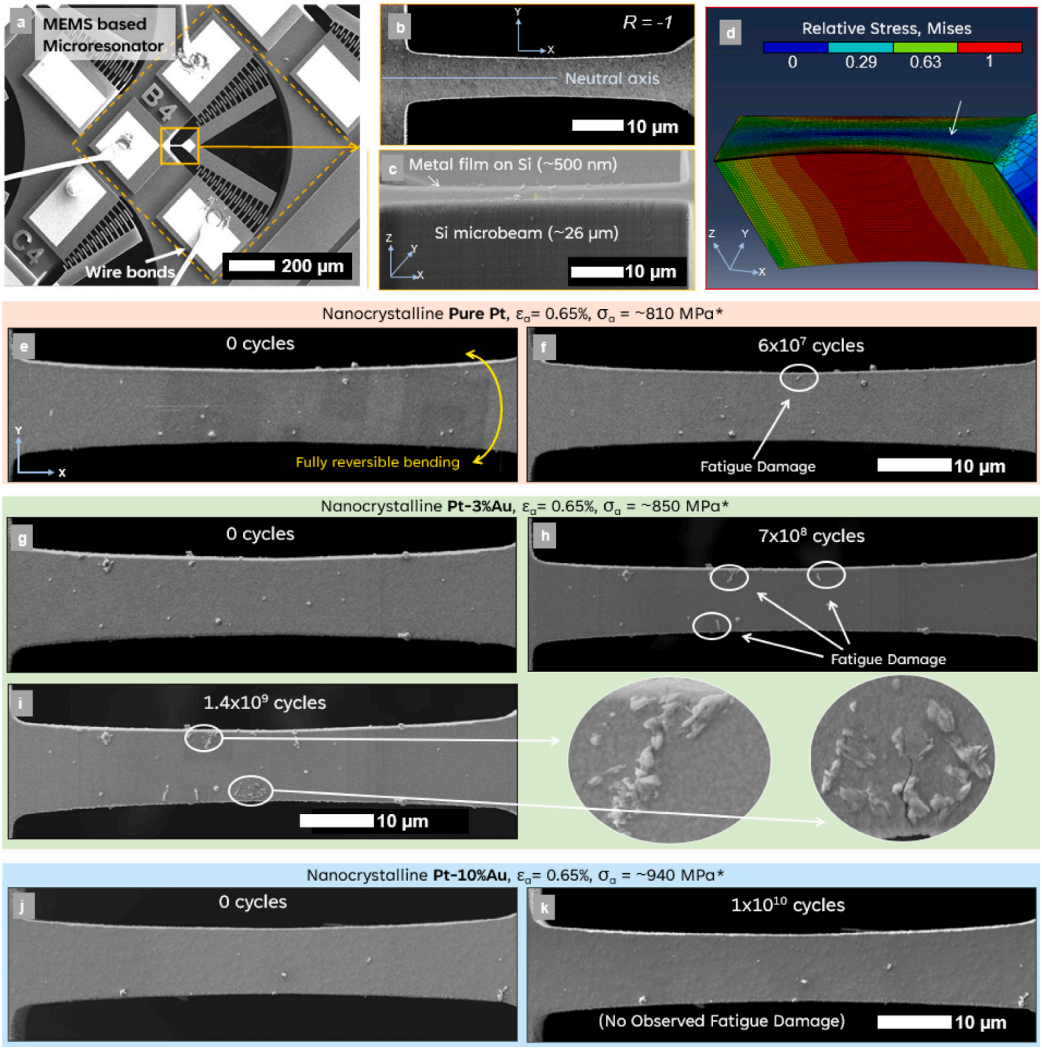

Fig. 1. Detecting the onset of fatigue damage using MEMS microresonators. (**a**) Si-MEMS microresonator chip, (**b**) top-down view of the microresonator beam, (**c**) oblique view of the microresonator beam, with an arrow showing the metallic thin film with a thickness of approximately 500 nm deposited on top of the 26 µm-thick microbeam, (**d**) FEA model of microresonator, (**e** and **f**) images of the pure Pt surface before and after fatigue loading, at a strain amplitude of 0.65%, (**g-i**) similar observations in Pt-3Au, but occurring after longer cycle counts, (**j-k**) no observable fatigue damage in Pt-10Au even after 10 billion cycles.

Results and discussion

Detecting the first signs of fatigue damage

Quantifying VHCF behavior in the gigacycle regime is challenging at any length scale [15]. To enable rapid testing, thin Pt-based films were deposited via physical vapor deposition (PVD) onto a Si-based microresonator carrier [16] (Fig. 1). Using electrostatic actuation [17,18], this microresonator can be driven at resonance (9800–10200 Hz), resulting in fully reversed cyclic bending. During fatigue testing, the metal-coated microresonator was driven at or near its resonance frequency under constant strain amplitude. The strain amplitude, determined from the angular displacement observed in the SEM, was maintained by compensating for any fatigue-induced damping through controlled adjustments in drive voltage. Motion at resonance was regularly verified in situ within the scanning electron microscope (SEM); the measured blur envelope of the comb structure confirmed the intended strain amplitude levels. Similar microresonator devices have previously been constructed entirely from silicon [19] or a monolithic metal [18,20]. The key distinction here is that any blanket film can be deposited onto the Si carrier, enabling high-throughput screening. The deposited metal must be thin enough so that the film strain is dominated by the larger Si device, as verified through finite element analysis (Fig. 1d). This device allows 1 billion cycles in 28 h, compared to several months required by conventional methods. Further details on the material, deposition process, and microresonator operation are provided in Methods.

To monitor fatigue damage evolution, we developed a custom automation script that controlled the SEM and the microresonator drive signal to periodically pause cycling and capture images of the sample gauge sections. These images were used to identify the initial onset of microscopic fatigue damage, which was correlated with subsurface grain growth and fatigue-induced extrusions. Fig. 1e-k presents SEM images showing the progression of fatigue damage for pure Pt, Pt-3Au, and Pt-10Au. Initial SEM images of each thin film (Fig. 1e,g,j) revealed surface irregularities, such as debris or deposition anomalies, serving as fiducials. During fatigue cycling, pure Pt and Pt-3Au developed emergent surface defects, including extrusions and cracks (Fig. 1f,h,i). These defects emerged in pure Pt after approximately 6×10^7 cycles (Fig. 1f), while Pt-3Au showed delayed damage onset, appearing after 1.2×10^8 cycles (Fig. 1h), with multiple defects observed at 7×10^8 cycles. Unlike conventional fatigue tests, which halt at the first catastrophic crack, these carrier-based tests permitted ongoing damage evolution after cracking (e.g., Fig. 1).

To assess the resistance to fatigue damage, we present a modified S-N curve in Fig. 2e, plotting the number of cycles to the onset of

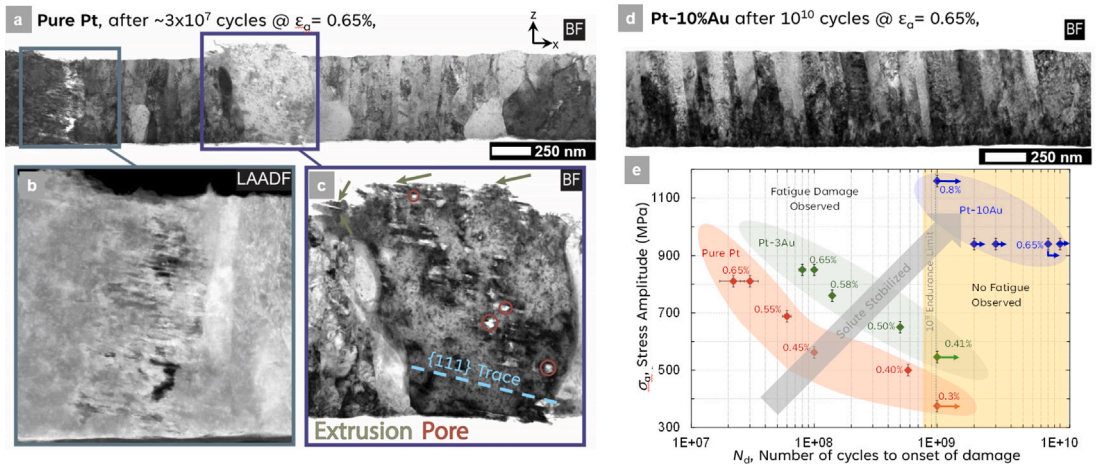

Fig. 2. Fatigue damage evolution and fatigue life curve. (**a**) Post-mortem cross-sectional Bright Field (BF) scanning transmission electron microscopy (STEM) image of the pure Pt film after 100 million cycles at 0.65% strain, with Low Angle Annular Dark Field (LAADF) STEM and BF-STEM images in (**b**) and (**c**) showing details of grain growth and subsequent fatigue damage. Arrows in (**c**) mark extrusions. (**d**) Post-mortem BF-STEM image after 10 billion cycles at 0.65% strain of the Pt-10Au film showing no observable fatigue damage. (**e**) Stress-Life (S-N) Curve of Pt, Pt-3Au, and Pt-10Au films tested on Si microresonators. The number next to each point indicates the maximum applied strain, and points with a right-facing arrow indicate run-outs where no fatigue damage was observed.

surface damage (N_d) on the x-axis instead of cycles to failure. This N_d metric, derived from in-situ monitoring, serves as a more sensitive indicator of extrusion formation. Tests that terminated without detectable surface damage are marked as run-outs with right-pointing arrows. Stress values are based on elastic estimates from applied strain (labeled above each data point) using moduli reported in Heckman et al. [14]. Crystal plasticity simulations based on EBSD data confirmed that the films are nearly isotropic, with Young's moduli of 140.6 GPa in the normal direction and 135.9 GPa in-plane, as analyzed in Supplemental. Pure Pt and Pt-3Au exhibited VHCF endurance limits of 0.41% and 0.3% strains at 10^9 cycles, respectively. In contrast, the Pt-10Au films significantly outperformed pure Pt and Pt-3Au, with no detectable surface damage even after one billion cycles at strain amplitudes of 0.80% (the maximum strain of the microresonators). Several tests were repeated, including a test at 10 billion cycles at a strain amplitude of 0.65%.

The surface features observed in the SEM after cycling are linked to the grain-growth process preceding fatigue failure in nanocrystalline metals [3,14,21]. To verify the association of these surface features with grain evolution, cross-sectional focused ion beam (FIB) liftouts were prepared at damage sites for post-mortem analysis. Cross-sectional TEM analysis confirmed that the silicon/Pt–Au interface remained intact after fatigue testing, with no evidence of interfacial cracks or delamination; instead, fatigue damage consistently appeared at the film surface in the form of extrusions. Fig. 2a reveals coarse grains beneath the extruded region in the pure Pt sample, surrounded by finer (as-deposited) grains. After fatigue-induced grain growth in Pt, the largest grains reached sizes of 400–500 nm (Fig. 2b and c). These larger grains exhibited distinct damage morphologies, with voids primarily located along {111} planes (indicated by the purple dashed line in Fig. 2c). Previous research has documented void formation in fatigued thin films beneath extrusions [22], but the exact mechanism remains unclear. One hypothesis posits that dislocation movement during fatigue loading generates vacancies that coalesce into voids [18,23]. Based on observations from Figs. 1 and 2, we surmise the following sequence of events: fatigue loading induces grain growth, followed by dislocation activity that forms persistent slip bands in larger grains. These slip bands create extrusions and intrusions at the surface, which grow as additional dislocations accumulate. When these surface features reach a critical size, they create effective notch-like stress concentrations that trigger the transition from crack nucleation to propagation. Concurrently, non-conservative dislocation activity leads to vacancy formation, and the coalescence of these vacancies into voids may further contribute to cracking. Further discussion of the fatigue damage mechanism is provided in Supplemental Note 3.

In contrast to the pure Pt and Pt-3Au cases, the absence of surface features after fatigue of Pt-10Au suggests a suppression of grain growth. Cross-sectional imaging of the Pt-10Au film after 10^{10} cycles confirmed a microstructure similar to the as-deposited state, with no observable grain growth, deformation substructure, or voids (Fig. 2d).

In addition to serving as a GB stabilizer, solute additions also contribute to the strengthening [24–26]. However, with an atomic radius only 5% larger than that of Pt, Au contributes an additional strength of only 70–80 MPa. For this reason, solute-enhanced fatigue resistance is believed to stem primarily from GB stabilization. Previous studies on PVD-deposited Pt–Au alloys have shown Au enrichment at GBs [11,14,27], which is associated with improved thermal stability [12]. However, atom probe microscopy has revealed a more complex scenario: some boundaries are depleted of Au, while others exhibit spinodal decomposition into Au-rich and Au-depleted zones [28]. Here, compositional maps on both as-deposited and fatigued samples were collected (Section "Material Characterization"). Our results indicated a nearly uniform distribution of Au throughout the microstructure, even with a few percent of reduced Au content at the GB. Nevertheless, several percent of Au remained present at the GBs. These results suggest that further improvements in fatigue resistance could be realized if solute atoms segregate preferentially to grain boundaries, thereby providing additional resistance to grain boundary migration. In the following section, we will demonstrate through atomistic modeling that even depleted GBs which retain some solute can still benefit from the stabilizing effect.

Atomistic origins of solute-stabilized fatigue resistance

Before examining the role of solutes in enhancing fatigue resistance, it is important to consider the fatigue-induced grain growth process in pure metals. Thermal coarsening of grains is often analyzed through Arrhenius atomic hopping at grain boundaries (GBs), driven thermodynamically by the excess free energy of curved GBs [29–31]. Alternatively, mechanical factors, such as disparate elastic strain energy in adjacent grains due to elastic anisotropy, can also motivate diffusive mechanisms [17,32–34]. Recent studies have shifted focus to the role of GB defects in boundary migration, particularly disconnections, which reconcile traditional views of grain growth with shear-coupled

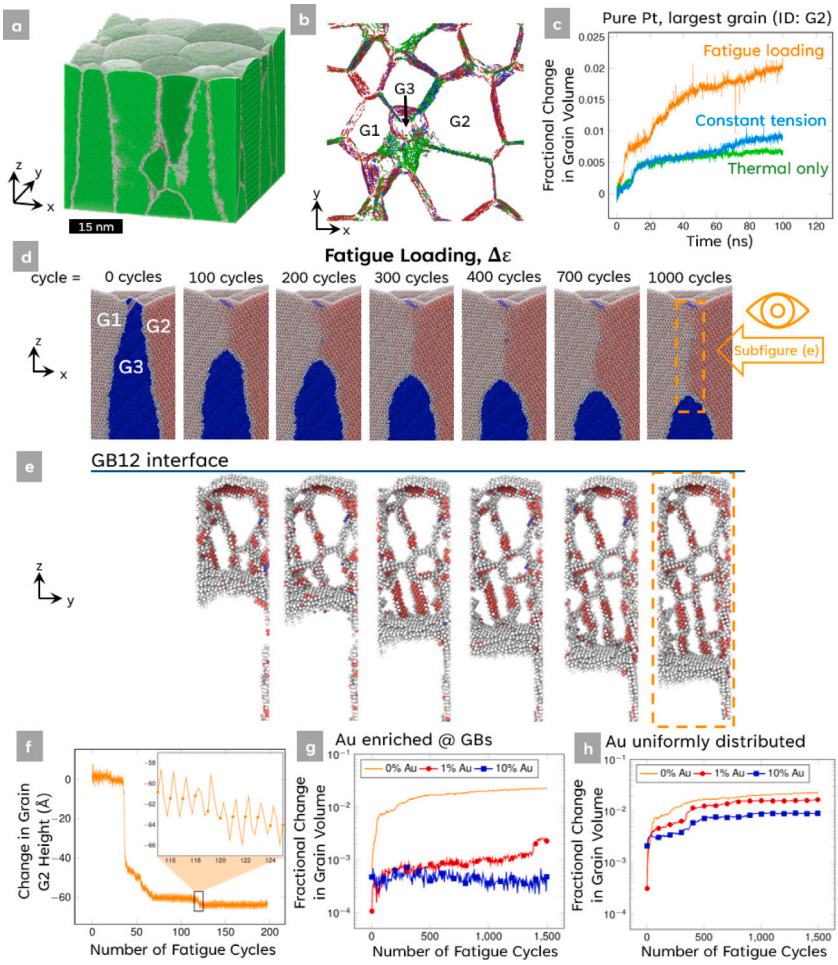

Fig. 3. Atomistic details of solute-modulated grain growth and cyclic ratcheting. (**a**) Atomistic cell representing grain size, shape, and crystal texture characteristic of films grown by the PVD process. (**b**) DXA-visualized defect content at the grain boundaries, with different colors representing unique dislocation character. (**c**) Fractional change in grain volume for the largest grain under three different stimuli. (**d**) A cross-sectional slice through the atomistic simulation reveals triple junction migration. (**e**) Viewing only the atoms that do not index as FCC on the GB12 interface. Red is HCP, blue is BCC, and gray is undefined. (**f**) The vertical migration of triple junction TJ123 is quantified revealing cyclic ratcheting (see inset, dots indicate the start of each cycle). (**g**) When solutes are enriched only at the GBs, the growth rate of the fastest growing grain is dramatically slowed, even with very small amounts of solute. (**h**) If the solute is uniformly distributed there is still a clear slowing of the grain-growth process, even for low solute concentrations.

migration processes [35]. A recent study demonstrated that disconnections subjected to thermal cycling can lead to net (asymmetric) migration of GBs through a process termed Brownian ratcheting [5]. This mechanism has also been suggested to explain grain growth driven by mechanical fatigue.

In this study, polycrystalline atomistic simulations were utilized to compare grain growth under thermal exposure (unloaded 300 K), monotonic strain (constant 0.65% strain at 300 K), and cyclic strain (+0.65 to −0.65% strain at 300 K) in both pure Pt and Pt with Au additions. Here, the simulated duration of all three scenarios was 100–150 ns, corresponding to 1000–1500 fatigue cycles; to our knowledge, this sets the record for fatigue cycling in an atomistic setting. Our own previous studies on pure metals with synthetic equiaxed microstructures were limited to 5 or 40 ns (50 or 200 cycles) [34,36]. Those prior studies had already demonstrated utility in predicting qualitatively similar grain-growth processes including the accelerating effect of cyclic loading over monotonic or purely thermal loading. Unlike prior MD studies that have focused exclusively on pure metals, the present simulations explicitly incorporate solute segregation and demonstrate its stabilizing effect on grain boundaries under cyclic loading, thereby providing direct mechanistic support for the experimentally observed suppression of fatigue damage in Pt–Au films. The current simulations were performed on microstructural digital twins generated via phase-field simulations of the PVD deposition process [37], combined with statistical sampling of experimental crystal textures (Fig. 3a and Section “Molecular Dynamics Simulation Method”). The relaxed grain structure comprised 25 grains and naturally formed native defect structures at the GBs (Fig. 3b). A dislocation extraction algorithm (DXA) [38,39] was used to identify specific defect types, although its application at GBs is dubious. Nonetheless, the visualized DXA defects resemble common GB defect structures.

Fig. 3c illustrates the fractional growth in the number of atoms associated with the largest grain (G2) in the simulated structure. This grain grows more than twice as fast under fatigue loading compared to the constant tension or unstrained purely thermal case. Similar observations were noted for the top five growing grains, as detailed in Supplemental Fig. S1. Cross-sections of the atomistic simulation provide further insight into the growth process (Fig. 3d). A shrinking grain (G3) is consumed as two adjacent grains (G1 and G2) pinch off G3, forming a new triple junction (TJ123). As a result, GB12 grows at the expense of GB13 and GB23, leading to downward migration of the TJ toward the seed layer. This behavior also occurs under thermal and constant strain stimuli, albeit at a slower rate (Supplemental Fig. S1). The growing GB12 establishes an organized network of GB defects that migrate, as illustrated in Fig. 3e. The formation and migration of the TJ are quantified in Fig. 3f, showing a sharp reduction in G3 height after 35

cycles, corresponding to the initial formation of GB12. Subsequently, TJ migration occurs in a discontinuous manner, characterized by periods of movement and dormancy. A closer examination of G3 height per cycle reveals evidence of ratcheting migration (inset in Fig. 3f, consistent with the recently proposed Brownian ratcheting mechanism [5]. In contrast, under thermal or constant strain conditions, G3 height did not exhibit such behavior. Here we define 'ratcheting' as the cyclic upward and downward oscillation of triple junctions observed exclusively under fatigue loading; the step-like changes seen under tension or thermal conditions are better described as dormancy events whereby migration temporarily halts until sufficient energy accumulates for motion to resume. Notably, the consumed grain had significantly higher stored elastic strain energy than the two adjacent growing grains (Supplemental Fig. S9), suggesting a potential driving force for boundary migration [40].

Next, we use this atomistic model to examine the role of solutes in stabilizing against fatigue-induced grain growth. Traditionally, solutes have been understood to contribute to thermal stabilization through mechanisms such as solute drag [41,42], Zener pinning at particles [43, 44], or by reducing the energetic cost of GBs [45]. While these mechanisms apply to perfect planar GBs, solutes may also stabilize boundary defects like disconnections. Recent studies by Hu et al. [6–8] utilized atomistic simulations to investigate this in the context of 1/6 ⟨121⟩ disconnections at a $\Sigma 3$ (111) GB in Cu with Ag solute additions. They found that disconnection mobility could be impeded or entirely halted depending on solute concentration and temperature, leading to the proposal of an interfacial defect diagram to explain this behavior.

In the atomistic simulations, several solute enrichment scenarios were explored, comparing Au concentrations of 1–10 at.% to a benchmark of pure Pt. In one scenario, randomly seeded Au atoms were equilibrated using a hybrid Monte Carlo Molecular Dynamics (MCMD) method, resulting in Au enrichment at the GBs and depletion in the grain interiors. For instance, for one of the concentration tested, after MCMD optimization, the atomistic structure with a global concentration of 1 at.% Au showed a local concentration of approximately 11 at.% Au at the GBs, while the bulk of the grains contained nearly no Au. Segregation was not uniform across all GBs and varied by GB type [11], with solute distribution potentially heterogeneous within a single GB [28]. The effect of solute content on grain growth is illustrated in Fig. 3g for this GB-enriched case. All Au concentrations resulted in grain growth being slowed by over an order of magnitude compared to pure Pt, with growth being nearly indistinguishable from the noise floor. This analysis of fatigue-driven grain growth was also conducted under thermal-only and constant-strain stimuli (see Supplemental Fig. S4), revealing similar solute stabilization effects, though less quantitatively pronounced.

In a second scenario, the solute was homogeneously dispersed throughout the simulation cell (as described in Section "Molecular Dynamics Simulation Method"), motivated by unexpected experimental observations that GBs were not enriched in solute (as described in Section "Material Characterization"). As shown in Fig. 3h, the stabilizing effect of the solute remained, though it was less pronounced. The effects observed under fatigue were qualitatively similar, but grain growth was reduced under thermal-only and constant-strain conditions (Supplemental Fig. S4). A third scenario examined the complete absence of solute at the GB while retaining it in the grain interiors. In this scenario, the solute did not stabilize the GB, resulting in a growth response similar to that of pure metal. We presume that GBs would eventually migrate into solute-rich regions and become stabilized, though the simulation duration did not reach that extent. This third scenario, devoid of Au at the GBs, was far more extreme than our experimental observations, where Au was nearly uniform and GBs were only slightly reduced in Au content.

The experimental Pt–Au films represent an intermediate state between the simulated extremes — neither complete segregation, uniform distribution, nor full depletion — where residual Au at the grain boundaries (5%–6%) remains sufficient to suppress grain growth and enhance fatigue resistance under cyclic loading.

It is also anticipated that Au atoms segregated at grain boundaries could influence boundary structure, potentially affecting partial dislocation emission and deformation twinning, and thereby indirectly contributing to grain boundary stability; however, in the present study neither atomistic simulations nor TEM analysis provided evidence of such an effect.

Expanded analysis of the results of the molecular dynamics simulations are provided in Supplemental Note 1.

Context and implications

The gigacycle fatigue resistance of the Pt–Au alloy reported here can be compared to the most fatigue resistant metals ever documented. For instance, bearing steels, known for their fatigue resistance, have recently achieved stress amplitudes of up to 850 MPa under very high cycle fatigue (VHCF) conditions with rare earth elemental additions [46]. In contrast, the Pt-10Au alloy sustained over 10^9 cycles at strain amplitudes up to 0.8%, corresponding to elastic stresses exceeding 1.1 GPa. This outcome is unexpected for a precious metal: state-of-the-art cold-worked Pt-20Ir wires used in pacemakers and other medical devices have a yield strength comparable to Pt-10Au (~1 GPa), yet they survive $<10^4$ cycles at 1.1 GPa [47]. While expensive alloying elements like Pt and Au are not suitable for large-scale structural applications, they do have significant technological relevance in such biomedical applications, as well as in electrical connectors and switches. More broadly, these findings suggest a roadmap for improving fatigue resistance in nanostructured alloys. However, solute-mediated grain boundary stabilization is not a general fatigue-resistance strategy for conventional alloys but is particularly effective in nanostructured metals where grain boundary processes dominate damage. The enhancement in fatigue resistance is attributed to two factors: (i) the fine nanocrystalline grain size impedes dislocation processes that lead to crack nucleation, and (ii) the solute reduces GB mobility, likely by pinning defects such as disconnections.

The current results differ from conventional fatigue tests in several ways that complicate rigorous quantitative comparisons. Factors such as the vacuum environment of the SEM, the 500 nm film thickness, the constraints of the attached substrate, and the bending strain gradient have been shown to influence fatigue response, as discussed in Supplemental Note 2. Nevertheless, the Pt-10Au alloy demonstrated substantial fatigue enhancement over pure Pt and Pt-3Au under identical conditions.

Another key distinction is the focus on the initial stages of damage prior to crack initiation. While many studies have quantified initiation life, this study detects the early signs of fatigue damage, in particular, slip steps on the surface, which have been linked to eventual crack nucleation [4]. This study does not address the propagation life required for crack growth from nucleation to failure. Generally, the propagation life of nanocrystalline metals is shorter than that of coarse-grained metals due to fewer toughening mechanisms. However, under high-cycle and very-high-cycle fatigue conditions, most fatigue life is consumed during the nucleation process, making enhancements in nucleation resistance critical for overall fatigue resistance.

One might question whether higher Au concentrations beyond 10% would provide additional benefits. At 100% Au, the material would not benefit, and even at 50% Au, phase separation could facilitate grain growth and crack nucleation. A few cursory fatigue experiments were also performed on a 33% Au alloy following the same protocols described in this study. That alloy still showed complete resistance to fatigue damage. Within the limits of the current method (maximum strain amplitude of 0.8%), the effects of 10% versus 33% Au are indistinguishable, but future studies at higher strain levels may clarify optimal Au content. It is also possible that the addition of Au alters the nature of grain boundary structures and influences the density

Table 1
PVD deposition parameters.

Adhesion material	Targeted adhesion thickness (nm)	Adhesion pressure (mTorr)	Adhesion rate (Å/min)	Material composition	Targeted material thickness (nm)	Pressure (mTorr)	Deposition rate (Å/min)	Total thickness (nm)
Cr	15	10	105	Pt	510	22	300	515.7
Cr	15	10	300	Pt-3Au	530	22	300	391.8
Cr	15	10	105	Pt-10Au	510	22	300	510.7

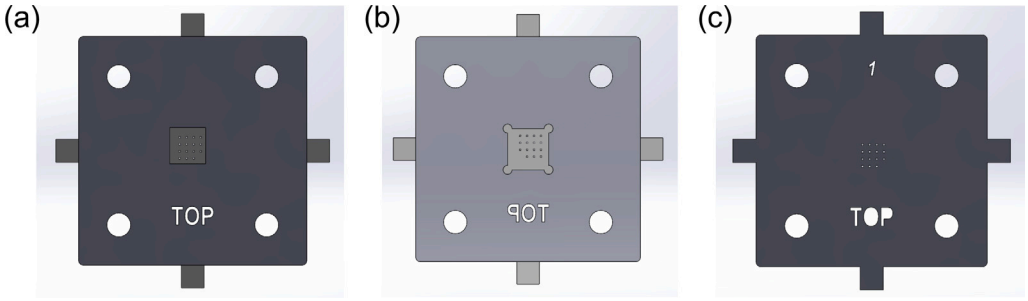

Fig. 4. Kapton mask for local metal deposition. (**a**) Top plate and mask viewed from above, (**b**) top plate and mask without the base plate viewed from below, (**c**) diagram of the Kapton mask.

of various defects, which may contribute secondarily to the observed stabilization. A detailed cataloging of grain boundary types in pure Pt versus Pt–Au films, however, is beyond the scope of the present work and would be a valuable direction for future studies.

Conclusions

In summary, this study offers a metallurgical strategy to stop fatigue damage entirely. Incorporating solutes in nanocrystalline metals enhances fatigue resistance by suppressing grain growth, a precursor to crack initiation. Molecular dynamics modeling confirmed that solute localized at GB defects impedes boundary mobility. This effect is most pronounced when solute segregates to the GB, though stabilization occurs even with uniform Au concentration, requiring higher overall solute levels. This study raises the possibility of a future where metals can be tailored to eliminate fatigue susceptibility.

Materials and methods

Material synthesis

Depositions of the pure Pt, Pt-3Au, and Pt-10Au thin films on top of microelectromechanical system (MEMS) devices were performed in a Unifilm DC magnetron sputtering system with a MeiVac sputtering gun, using a vertical sputtering throw distance of 0.4". The Unifilm Technology PVD-301 System Control software was used for system control. Deposition was performed with the sample and sputtering gun oriented to maximize normal incidence of particles on the sample as to maximize the resulting film density. The pressure in the deposition chamber was pumped down to below a base pressure of 5×10^{-7} Torr. An adhesion layer of 15 to 20 nm of Cr was deposited under a working gas inflow of 10 mTorr Ar, after which one of a set of mixed Pt–Au alloy targets were used to deposit the desired film. See Table 1 for specific deposition parameters. The total film thicknesses provided in Table 1 were measured on flat witnesses. The compositions deposited from the alloy targets were verified via Wavelength Dispersive Spectroscopy (WDS).

As it was necessary to deposit the thin film on top of the mechanical test region of the MEMS device while avoiding the formation of short circuits with other components, a mask was used to control the deposition domain. Fig. 4 provides diagrams of the alumina clamp which were used to securely hold the MEMS device in place during deposition. A Kapton mask with a thickness of 0.005" was prepared using a laser cutter to facilitate the alignment and exposure of only the desired region of the MEMS device. A diagram of the mask is provided in Fig. 4c, while Fig. 5 shows the MEMS microresonator device with a box indicating the masked region where the thin film was deposited.

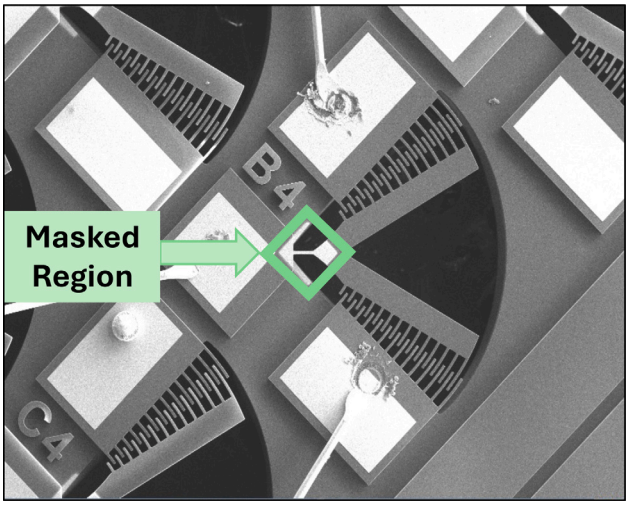

Fig. 5. Si-MEMS microresonator device with a box indicating where a Kapton mask was used to define where the metallic thin film would be deposited.

One Pt-33Au sample was prepared using a turbomolecular-pumped Kurt J. Lester Inc. PVD-200 system equipped with multiple 7.5 cm diameter TORUS™ Mag Keeper Sputter guns via co-sputtering of pure Pt and pure Au targets. Simultaneous co-sputtering of Pt and Au onto the MEMS device on a fixed (non-rotating) stage permits deposition of arbitrary alloy compositions, albeit with an understanding that different working distances and gun voltages to those from the Unifilm system must be used. The correct set of deposition conditions were identified using the SiMTRA program [48] which models the transport of sputtered atoms through the Ar working gas. SiMTRA simulations allow the user to construct a model of the vacuum chamber and its contents, and then simulate the trajectory of sputtered atoms until they collide with one of the modeled surfaces. The orientation and position of the MEMS device target and the process parameters were adjusted

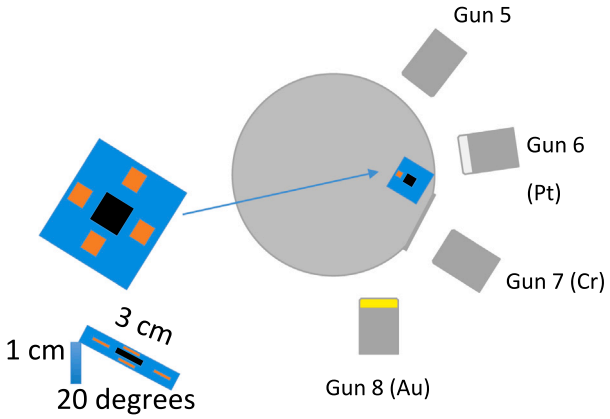

Fig. 6. Schematic diagram of the deposition chamber inside the PVD-200 system.

based on a SiMTRA simulation for the deposition of a Pt-30Au film, with a schematic of the interior of the deposition chamber shown in Fig. 6. The simulations performed for this work also utilized calibrations and calculations previously performed for Pt–Au co-depositions in the PVD-200 system [49].

The co-deposition was performed under a 3 mTorr Ar flow into a vacuum of approximately 10^{-8} Torr. All of the guns in the chamber were angled toward the substrate at a 20° angle from the surface normal of the substrate. An adhesion layer of Cr was deposited for 100 s with the Cr Gun set to 100 W. After the deposition of the adhesion layer, simultaneous co-deposition of Pt and Au was performed for 1300 s with the Pt gun set to 150 W and the Au gun set to 110 W. Four ride-along Si with oxide witnesses were attached to the deposition mask and were compositionally verified via WDS.

Material characterization

Cross-sectional thin foil specimens of the as-deposited and tested Pt and Pt-10Au films were prepared using the focused ion beam (FIB) lift-out process. The untested and tested samples were examined using a Thermo Fisher Scientific Themis Z at 300 kV. All samples were imaged using low angle annular dark field (LAADF) and bright field (BF) imaging in scanning transmission electron microscopy (STEM). The LAADF and BF imaging was done with an angular annular detector range of 22 to 131 mrad and 18 mrad, respectively, with a probe semi convergence angle of 6.0 mrad. The as-deposited nanocrystalline microstructures were determined to be composed of columnar grains with diameters between 30 to 50 nm via STEM (Fig. 7).

Earlier studies have demonstrated that in nanocrystalline Pt–Au thin films fabricated via PVD, Au tends to segregate to grain boundaries, contributing to their thermomechanical stabilization [12,50,51]. However, in the present work, high-resolution compositional analysis revealed grain boundaries that were unexpectedly depleted of Au, suggesting a fundamentally different segregation behavior or kinetic pathway during deposition.

Cross-sectional and plan-view thin foil specimens of the as-deposited Pt-10Au films were prepared utilizing a Thermo Fisher Scientific Helios NanoLab 660 dual-beam focused ion beam-scanning electron microscope (FIB-SEM). A schematic showing the specimens orientations taken from the depositions can be seen in Fig. 8a. The specimen that was fabricated normal to the deposition direction (cross-section) is outlined in purple whereas the specimen oriented along the viewing direction (plan-view) is outlined in pink in Fig. 8a. The preparation of the samples was done with bulk material removal at 30 kV and thinning of the film was done at 5 kV both with glancing angles between 1.5 to 2.0°.

Imaging and compositional measurements were performed using a Thermo Fisher Scientific Themis Z equipped with a 4-quadrant SuperX Energy Dispersive X-ray Spectrometer for Energy Dispersive X-ray (EDS). STEM EDS measurements and high-angle annular dark field (HAADF) images were collected with a detector range of 51 to 200 mrad with a probe convergence angle of 25.2 mrad. Subsequent EDS data was analyzed using Thermo Fisher Velox software using a Gaussian blur prefilter with a sigma value of 1.0.

The EDS atomic fraction composition maps for Pt and Au showing the absence of solute segregation for the as-deposited Pt-10Au film in both the cross-section and plan-view orientations can be seen in Fig. 8d-g and Fig. 8h-k, respectively. The composition maps of the cross-section in Fig. 8e-f reveal no apparent segregation of Au to the grain boundaries throughout the thickness of the film. A compositional line profile across a grain boundary (GB) within the composition map (blue rectangle) can be seen in Fig. 8g and shows no obvious enrichment of Au near the boundary, nor depletion of Pt. The plan-view specimen composition maps clearly show an enrichment of Pt and a depletion of Au in the grain boundaries in Fig. 8i and Fig. 8j, respectively. A compositional line profile across a GB, Fig. 8k, from the composition maps (blue rectangle) shows the Au depletion and subsequent Pt enrichment across a GB. To better understand the composition profile across the grain boundaries (GBs) in the post-fatigue specimens, EDS maps were collected across the thin film and some select boundaries, as shown in Fig. 9.

While the STEM cross-sections provide the most convincing evidence of fatigue-induced grain growth, or its absence in Pt-10Au, statistical analysis of grain size distributions also corroborates this observation. Upon examination of the histograms in Fig. 10 (a)&(b) for the top portions of the pure Pt films show an almost doubling of the grain size, with abnormally large grains contributing to a significant upper tail in the grain size distribution. For the Pt-10Au there is little change in the grain size after fatigue.

Microresonator fatigue testing method

The fatigue tests rely on in-plane vibration of a microresonator, as depicted in Fig. 1a in the main text. The electrically grounded microbeam is actuated via electrostatic forces by applying an AC signal (with no offset) to the comb structure on one side of the microresonator (using a combination of an Agilent 33220 A 20 MHz waveform generator and an AVTECH-110G high voltage amplifier). The microresonators are driven near their first resonant (bending) frequency of approximately 10 kHz. With minimal damping and a high Q-factor (> 2500), they follow the equation of motion for a lateral rotational oscillator. When the device oscillates it experiences angular acceleration which requires torque proportional to the moment of inertia, effects which give rise to the angular rotation θ and a fully reversed bending strain within the microbeam, as measured via the blur envelope of the comb drive.

At the beginning of each fatigue test, an optical calibration was conducted. During this calibration, the distance was measured between the edge of a comb's finger at rest (without load) and the edge of a comb's finger vibrating at its resonance frequency (maximum θ_0) as illustrated in Fig. 11a and b. The blur that can be seen in Fig. 11b results in an uncertainty in the comb position, which equates to an uncertainty in the measurement of θ_0. The magnitude of this uncertainty is measured by quantifying the amplitude of the blur of the stationary edges in the SEM images, indicated by the white arrow in Fig. 11b, which results in an uncertainty in θ_0 of approximately 1 mrad. The strain amplitude is calculated using the relationship derived from Finite Element Analysis (FEA) simulations of the microresonator, which is shown in Fig. 11c. All strain amplitudes in this study correspond to the strain amplitude at the edge of the microbeam, which corresponds to the position of highest stress seen in Fig. 1d of the main text. The

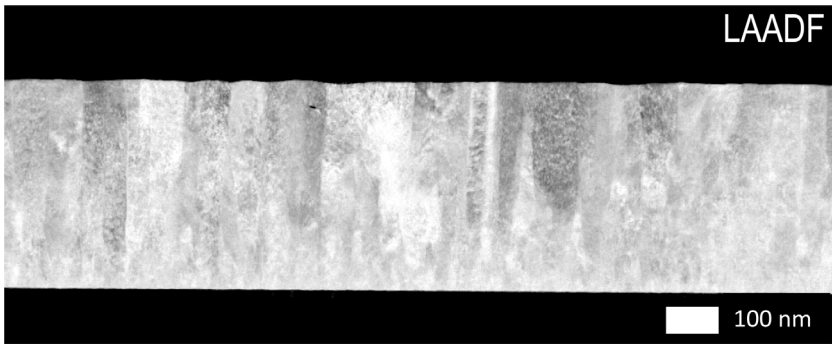

Fig. 7. Cross-sectional STEM-LAADF image of the as-deposited Pt-10Au thin film.

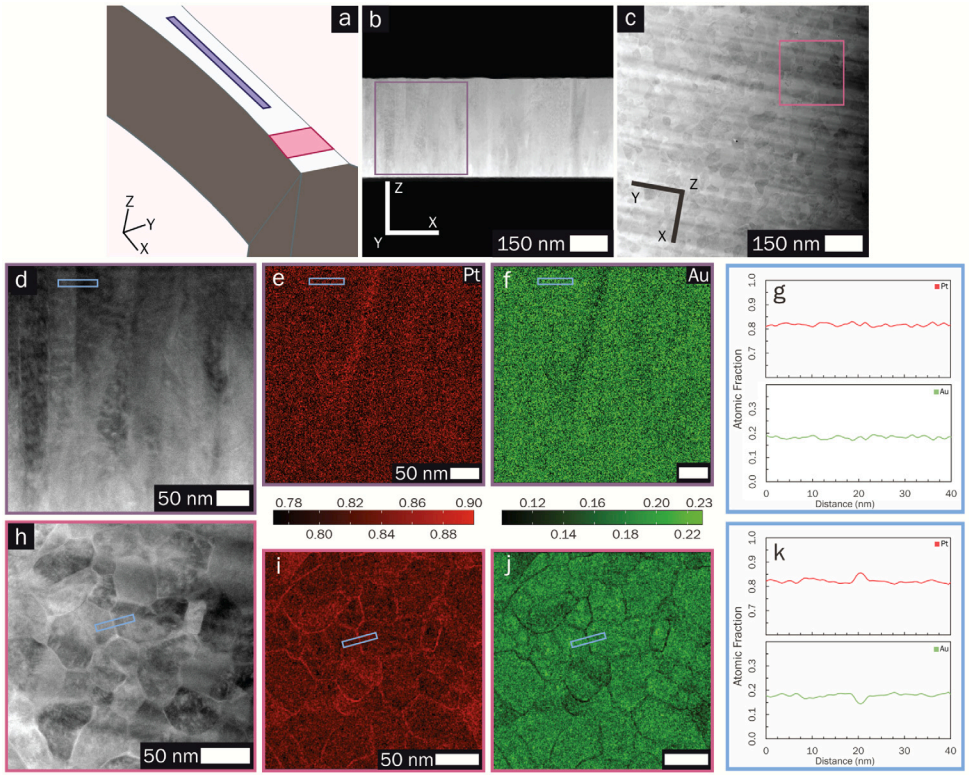

Fig. 8. Solute segregation maps. EDS results from specimens fabricated from the as-deposited Pt-10Au on the Si-MEMs device are shown here. A schematic showing the cross-section (purple) and the plan-view (pink) orientations from the device shown in (**a**). The cross-section data is shown in (**b**) & (**d-g**) and the plan-view data shown in (**c**) & (**h-k**). The cross-section and plan-view regions in (**d-f**) and (**h-j**) are outlined in the HAADF images in (**b**) and (**c**), respectively. The STEM-HAADF images, EDS atomic fraction composition maps, and composition line profiles for the cross-section and plan-view specimen shown in (**d**) & (**h**), (**e-f**) & (**i-j**), and (**g**) & (**k**), respectively. The blue rectangles in the HAADF-images and the composition maps show the regions for which the line profiles were extracted from the EDS composition maps.

uncertainty in the strain is approximately 0.015% due to the uncertainty in the angle of rotation at resonance. The tests were interrupted every 15 min (approximately equivalent to 9 million cycles) to examine the samples for fatigue-induced damage. In the very high-cycle fatigue region (here defined as more than 100 million cycles), the uncertainty in the number of cycles measured is roughly 9 million cycles. Single-crystal Si microbeams, which do not exhibit fatigue damage in vacuum up to strain amplitudes of 2%, provide an ideal elastic substrate for probing the fatigue evolution of metallic thin films. This allows us to isolate and study the role of metal microstructure, using the underlying Si beam as an elastic carrier to impose strain on the metal film.

The in-situ SEM fatigue tests were conducted in a JEOL IT500 HR SEM, where electrical feedthroughs apply the electrostatic force to the actuation comb drive. The fatigue tests were conducted in the fully reversible bending (R= −1) mode with strain amplitudes ranging from 0.2% to 0.65% strain. Note that the strain amplitude range mentioned here refers to the maximum strain at the central edge of the beam, which was predicted using FEA simulations (Fig. 1d in the main text for a visual representation). The stress amplitude is reported as reference values, estimated from strain using the modulus obtained from our prior work on the monotonic tensile properties of nanocrystalline pure Pt and Pt-10Au [52]. Predictions from the FEA simulation indicate maximum stresses of 810 MPa and 942 MPa, respectively. These stress estimates are only appropriate because the metal films are assumed to remain elastic prior to the onset of plastic damage, an assumption that was further supported by the lack of shift in resonant frequency. For macroscopic fatigue tests, the fatigue limit of the sample typically refers to the number of cycles required to propagate a crack until full separation. In this study, the fatigue limit is defined by the first

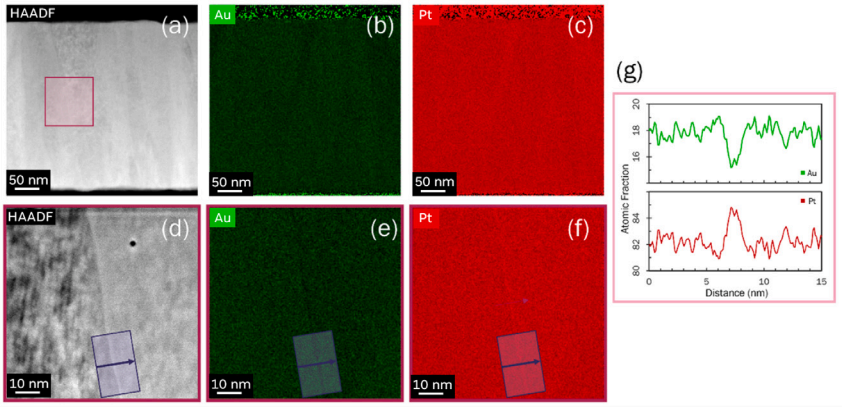

Fig. 9. A typical grain boundary after fatigue of the Pt-10Au film, imaged via STEM HAADF (**a** & **d**) and EDS (**b-c** & **e-f**). HAADF-STEM & EDS spectrum images (**a-c**) of the entire film cross section shows no appreciable variation in the Au solute across grain boundaries. Magnified spectrum images of an edge-on GB (**d-f**) shows no enrichment of gold across the grain boundary, but mild depletion. A composition profile crossing the grain boundary in (**g**) shows the integrated line profile across the purple box in (**d-f**).

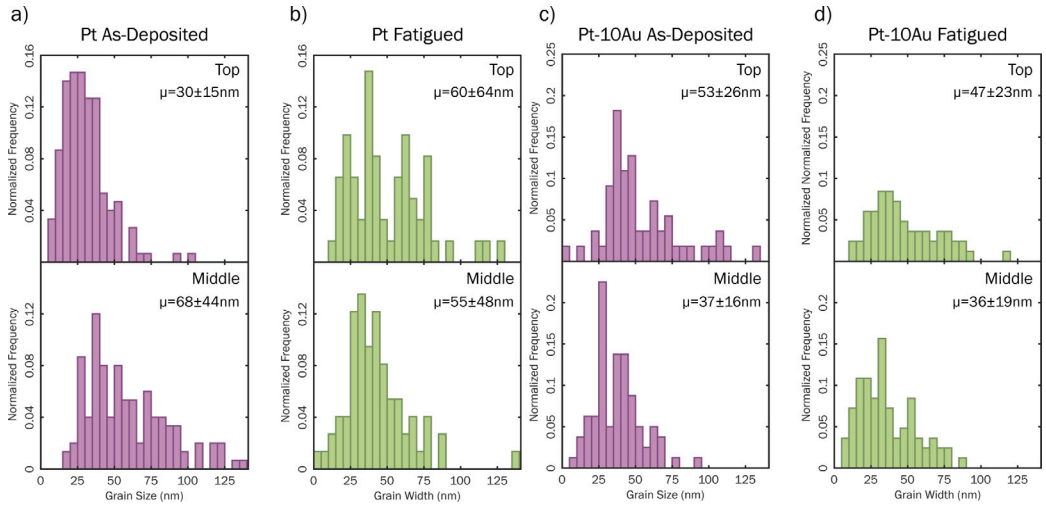

Fig. 10. The stacked histograms show the grains size distributions between the top and middle portion of the thin film deposition. The histograms for the As-deposited Pt (**a**), fatigued Pt at 0.65% strain amplitude for 60 million cycles (**b**), as-deposited Pt-10Au (**c**), and fatigued Pt-10Au at 0.65% for 10 billion cycles (**d**). The mean grain size and standard deviation are also included within the plots.

observation of fatigue damage on the surface of the microbeam in the form of extrusions, as shown in Fig. 1e-k in the main text.

To ensure that the high-frequency fatigue tests did not induce significant thermal effects that could alter the microstructure, thermoreflectance measurements were conducted. These tests were specifically aimed at decoupling any temperature-related changes from the fatigue-driven microstructural evolution. An infrared (IR) camera was employed to monitor the surface temperature of the sample in real-time during the test. The MicroSanj NT-220 thermoreflectance system was used and operated in steady-state mode on a 20 °C temperature-controlled stage with a $\lambda = 532$ nm LED as the probe light source. Even after 15 min of continuous operation (corresponding to approximately 9 million cycles at the system's resonance frequency of 10216 kHz) the recorded temperature rise was minimal, reaching only about 11 °C (Fig. 12). This negligible increase confirms that self-heating due to cyclic loading at high frequencies is insignificant under the current test conditions and is unlikely to influence the observed fatigue behavior or microstructural changes.

Calibration of the thermal conductance coefficient (C_{th}) was performed on-stage over the temperature range of 20 to 120 °C. Thermal coupling between the MEMS device and the stage was achieved using thermal paste, aluminum spacers, and mechanical clamps. The surface temperature of the device was monitored using a fine-gauge thermocouple directly in contact with the MEMS surface, yielding readings in the range of 22 to 103 °C due to non-ideal thermal coupling. The average value of C_{th} obtained on a Pt–Au alloy device was -1.05×10^{-4} °C, which is in reasonable agreement with previously reported values -0.6×10^{-4} °C [53]. Each measurement included a secondary thermocouple placed a few hundred micrometers from the energized resonator. Across all heating durations (30 to 900 s), the temperature increase within the region of interest (ROI) remained below 15 °C and spatial temperature variation was within the standard deviation, indicating minimal thermal gradients. An out-of-frame thermocouple showed no detectable temperature change, confirming negligible heating (less than 15 °C) due to resonator operation (Fig. 12).

Finite element method

A three-dimensional (3D) finite element model was developed using Abaqus to simulate the mechanical response of microresonators under small displacement bending. The analysis was quasi-static, displacement-controlled, and assumed linear elasticity. The complete geometry of the microresonator shown in Fig. 1(a), including the supporting frame, cantilever beam, and the thin film layer deposited atop the beam,

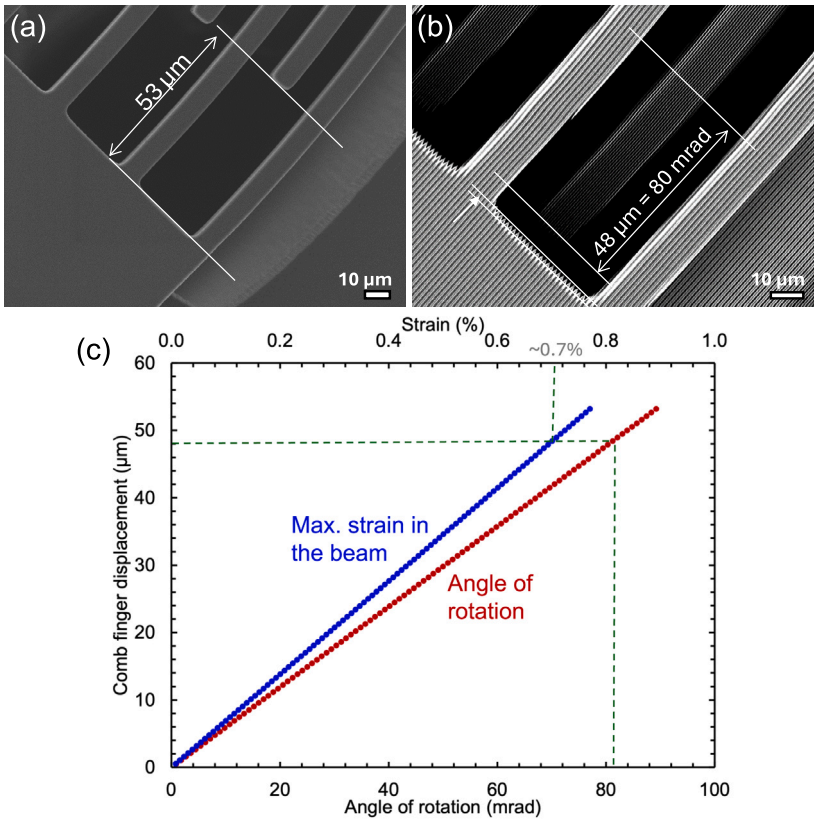

Fig. 11. Displacement amplitude analysis. (**a**) Comb finger position prior to starting the test, (**b**) Comb finger displacement during the test. Total displacement translates to strain in the microbeam according to the chart shown in (**c**). (**c**) Relation between the comb displacement, the angle of rotation, and strain in the microbeam, calculated using FEA.

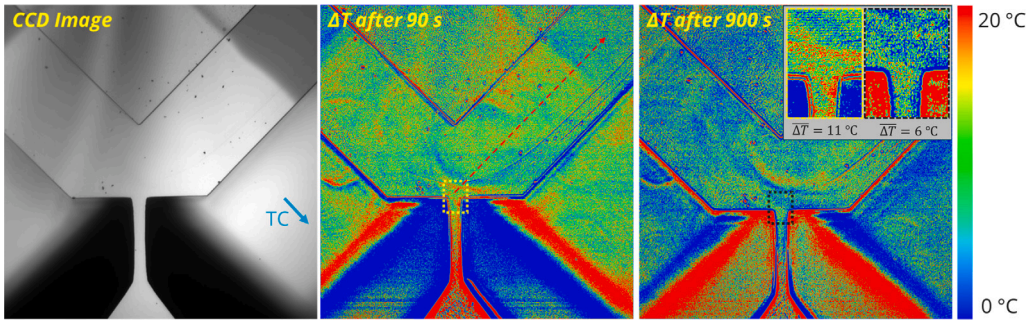

Fig. 12. Temperature change before and during the test determined via thermoreflectance measurements.

was modeled in full detail. The bulk of the resonator (V-structure and comb structures) were modeled with approximately 250,000 C3D8R (linear 8-node elements) elements. The microbeam and the thin film deposited on top were also modeled with 250,000 C3D8R elements each. The material properties of single-crystal silicon were assigned to the entire structure, with a Young's modulus of 170 GPa and Poisson's ratio of 0.28, as the mechanical response is dominated by the silicon substrate. All degrees of freedom were fully constrained at the base of the microbeam and resonator to accurately replicate the fixed boundary conditions observed in the actual device. The simulation involved incrementally increasing the angular deformation of the V-shaped structure in Fig. 1, with the resulting maximum strain at the thin film region above the microbeam recorded. As the system behaves elastically and the strain is continuous across the beam-film interface, the specific material of the thin film does not influence the strain outcome. This FEM model allowed for a direct correlation between the applied rotation angle θ and the maximum strain in the film.

Molecular dynamics simulation method

Atomistic simulations were performed using the open-source molecular dynamics simulation code LAMMPS (Large-scale Atomic/Molecular Massively Parallel Simulator) [54]. The Embedded Atom Method (EAM) interatomic potential for the Pt–Au alloy system developed by O'Brien et al. [51] was used for all of the molecular dynamics simulations performed for this work. This interatomic potential was fitted to accurately reproduce interatomic forces for the pure metals as well as mixtures of the two elements, as well as point defect formation energies, (100), (110), and (111) surface energies, the intrinsic stacking fault energy, and the segregation energies of either element at free surfaces, grain boundaries, and stacking faults. This potential has been used to study segregation in nanocrystalline systems [51] as well as segregation patterning around disconnections [55]. For all of the molecular dynamics simulations performed for this work, a standard timestep of 1 fs was used.

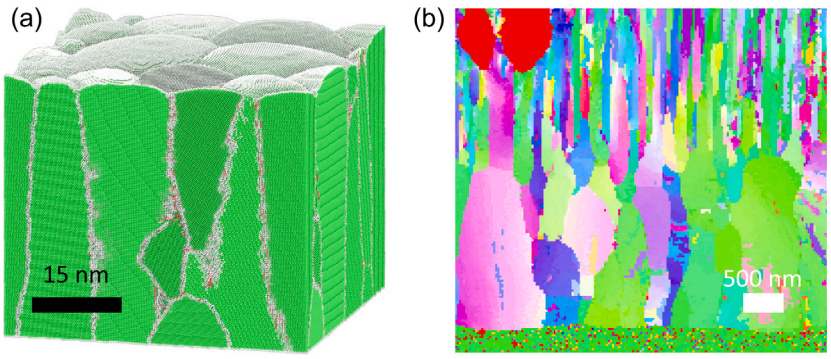

Fig. 13. Creation of the polycrystalline atomistic model. (**a**) Rendering of the atomistic structure where atoms are colored according to crystal structure, where green are FCC, red are HCP, and white are disordered. (**b**) ACOM orientation map of a thicker Pt-10Au thin film created for a previous study [11]).

Nanocrystalline thin film atomistic structures were created following the methodology established in Vizoso et al. [56] for the creation of atomistic nanoporous structures, with some modifications to account for the creation of a polycrystalline system. An image showing one of the final atomistic structures is provided in Fig. 13a. First, a phase field model that combined the formation of a thin film via PVD [57] and grain growth in polycrystalline systems based on work by Ahmed et al. [58] was used to generate a 3D voxelized structure of a polycrystalline thin film. This voxelized structure was converted into a mesh file containing only grains and no grain boundaries using a thresholding modifier in the Paraview data visualization software. A mesh-editing software was then used to rescale the mesh file such that the final atomic structure would have dimensions approximately equal to 50x50x40 nm. After rescaling the dimensions of the mesh, the mesh editing software was also used to create isolated mesh files for each of the individual grains, and these grain meshes were slightly scaled up in size to eliminate any gaps between grains that had formed during the thresholding and mesh creation processes. These meshes were then filled with atoms in an FCC lattice using NANOSCULPT [59]. The Pt lattice parameter of 3.92 Å was used to define the FCC lattice, and the lattice orientation was sampled from a set of experimentally measured grain orientations measured using Automated crystal orientation mapping (ACOM) in a Pt-10Au thin film deposited via PVD that had been created and analyzed for a previous study [11], shown in Fig. 13b. While this thin film is substantially thicker than the films examined in this study, the deposition methods were similar; therefore, it is believed that the distribution of grain orientations should also be similar between the two sets of films. After merging all of the individual grains into a single polycrystalline structure, the `overlap` version of the `delete_atoms` modifier within LAMMPS was used to ensure that there were no atoms closer than 2.5 Å from each other at the grain boundaries. This cutoff of 2.5 Å was selected since it is slightly below the first nearest neighbor distance for the Pt FCC lattice. This resulted in a nanocrystalline atomistic structure containing approximately 6.9 million atoms in 25 uniquely oriented grains, with periodic boundaries in the plane of the thin film.

Prior to use in any additional simulations, the pure Pt nanocrystalline structure was equilibrated in the following fashion. First, a region of atoms 15 Å-thick at the bottom of the film was frozen using the `setforce` command in LAMMPS. Then, an energy minimization was performed using the conjugate gradient method with an energy stopping tolerance (unitless) and force stopping tolerance (eV $Å^{-1}$) of 1.0×10^{-6} with the `fix box/relax` command in LAMMPS being used to perform the energy minimization under a zero-pressure condition across the periodic boundaries in the plane of the film. All atoms besides those included in the frozen region at the bottom of the film were then randomly assigned a velocity to set the temperature of the film to 10 K using the `velocity create` command in LAMMPS. The temperature of the film was then raised from 10 K to 300 K over the course of 200 ps under an NPT ensemble with the pressure in the periodic dimensions of the film (X and Y axes of the simulation cell) being maintained at zero. Then, the temperature of the film was raised from 300 K to 400 K over the coarse of 50 ps under an NPT ensemble set to zero pressure in the periodic dimensions, and then quenched from 400 K to 300 K over the coarse of 200 ps under an NPT ensemble set to zero pressure in the periodic dimensions.

Two sets of Pt–Au alloy structures with 1, 3, 5, and 10 atom % Au were created according to the following steps using the same pure Pt polycrystalline structure described above as the initial state. First, the desired fraction of atoms within the equilibrated Pt structure were randomly selected and their type was changed to Au. These randomly arranged structures were used as the initial states for simulations of solid solution structures, while the segregated structures were prepared according to the following additional steps. A frozen region 15 Å-thick at the bottom of the film was created using the `fix setforce` command in LAMMPS. A Monte Carlo Molecular Dynamics (MCMD) simulation was performed using the `fix atom/swap` command in LAMMPS with the `semi-grand` flag set to `no` to allow the randomly distributed Au atoms to move around the system and find lower energy sites. Atom swaps were not allowed to occur in the frozen region at the bottom of the structure or in a thin region containing the top surface of the film. The MCMD simulation was performed under an NVE ensemble with the system temperature being maintained at 10 K using a Langevin thermostat applied to all of the atoms outside of the frozen region. This simulation was performed using alternating MC and MD steps. During the MC steps, 100 Pt and Au atoms had their positions swapped, with each swap having a probability of being accepted based on the temperature of the system, which was set to 10 K. During the MD steps, atom positions were evolved under the NVE ensemble and the Langevin thermostat. The number of MCMD steps varied depending on the concentration of Au, as more steps were required for all of the Au atoms to find lower energy positions as the number of Au atoms in the structure increased. For the 1% Au structure, approximately 15 million atom-swap attempts were required to approach the minimum energy state, while for the 10% Au structure, approximately 55 million atom-swap attempts were required. After the total system potential energy had approached a plateau, each of the Pt–Au alloy structures had their temperatures increased from 10 K to 300 K under an NPT ensemble over the coarse of 100 ps with the pressure set to zero in the periodic dimensions of the thin film.

Simulations were performed with three different applied loading conditions: fatigue loading, static pure tension, and a thermal hold at 300 K. Fatigue simulations of the pure Pt, Pt-1Au, Pt-3Au, Pt-5Au, and Pt-10Au nanocrystalline thin film structures in solid solution or with GB segregation were performed in the following manner. All fatigue simulations were performed under an NVT ensemble maintained at 300 K with a frozen region 15 Å-thick at the bottom of the cell that had all of the forces on the atoms in the region set to zero using

the `setforce` command in LAMMPS. The `fix deform` command was used to sinusoidally adjust the x-dimension of the simulation box between maximum compressive and tensile strain states of 0.65%. The period of this oscillation was set to 100 ps, with the number of cycles performed varying depending on the structure.

Static pure tension simulations were performed for the pure Pt, Pt-1Au, and Pt-10Au solid solution and GB segregated structures. These simulations were performed under an NVT ensemble maintained at 300 K, with a frozen region 15 Å-thick at the bottom of the cell that had all of the forces on the atoms in the region set to zero using the `setforce` command. The `fix deform` command was used to linearly apply tensile strain in the x-dimension of the simulation cells, up to a maximum strain of 0.65% over the coarse of 50 ps. After the tensile strain had been applied, the structures were allowed to evolve under an NVT ensemble maintained at 300 K for 100 ns.

Simulations with a static hold at 300 K with no applied strain were performed for the pure Pt and Pt-10Au solid solution and GB segregated structures. These simulations were performed under an NVT ensemble maintained at 300 K with a frozen region 15 Å-thick at the bottom of the cell that had all of the forces on the atoms in the region set to zero using the `setforce` command. These structures were allowed to evolve at 300 K for a simulation duration of 100 ns.

Grain orientations and phase fractions were tracked using the `polyhedral template matching` modifier [60] in OVITO. The `grain segmentation` modifier in OVITO was used to measure the number of atoms within each grain at the middle point and the end point of each fatigue cycle (or every 50 ps for non-fatigue simulations), with a minimum grain size threshold of 2000 atoms. Visualization and quantification of the dislocation structure within grain boundaries was performed using the `DXA` modifier [38,39] in OVITO.

CRediT authorship contribution statement

Manish Jain: Writing – review & editing, Writing – original draft, Visualization, Methodology, Investigation, Formal analysis, Data curation. **Daniel Vizoso:** Writing – review & editing, Methodology, Formal analysis, Data curation. **Alejandro Hinojos:** Visualization, Methodology, Investigation, Formal analysis. **Alejandro Barrios:** Methodology, Investigation, Formal analysis. **Kyle R. Dorman:** Writing – review & editing, Methodology, Investigation. **Yichen Yang:** Writing – review & editing, Methodology, Investigation, Formal analysis. **David Adams:** Writing – review & editing, Supervision, Investigation, Funding acquisition, Formal analysis. **Khalid Hattar:** Writing – review & editing, Supervision, Conceptualization. **Olivier Pierron:** Writing – review & editing, Supervision, Investigation, Formal analysis. **Rémi Dingreville:** Writing – review & editing, Supervision, Methodology, Formal analysis. **Brad L. Boyce:** Writing – review & editing, Supervision, Resources, Methodology, Investigation, Funding acquisition, Formal analysis, Conceptualization.

Funding

M. J., D. V., A. H., A. B., K. R. D., D. L. M., R. D., and B. L. B. are supported by the United States (U.S.) Department of Energy (DOE) Office of Basic Energy Sciences (BES), Division of Materials Science and Engineering. Y. Y. and O. P. gratefully acknowledge support from National Science Foundation through award number 2224372. The experimental and computational resources for this work are supported in part by the Center for Integrated Nanotechnologies, an Office of Science user facility operated for the U.S. Department of Energy. This article has been authored by an employee of National Technology & Engineering Solutions of Sandia, LLC under Contract No. DE-NA0003525 with the U.S. Department of Energy (DOE).

Declaration of competing interest

The authors declare the following financial interests/personal relationships which may be considered as potential competing interests: Brad Boyce reports financial support was provided by US Department of Energy Basic Energy Sciences. Olivier Pierron reports financial support was provided by National Science Foundation. If there are other authors, they declare that they have no known competing financial interests or personal relationships that could have appeared to influence the work reported in this paper.

Acknowledgments

The authors would like to thank Nathan Heckman from Sandia National Laboratories for providing feedback and insightful comments during the preparation of this manuscript. The authors would also like to thank Ryan Schoell for his provision of ACOM data and Christian Harris for his WDS measurements. The employee owns all right, title, and interest in and to the article and is solely responsible for its contents. The United States Government retains and the publisher, by accepting the article for publication, acknowledges that the United States Government retains a non-exclusive, paid-up, irrevocable, worldwide license to publish or reproduce the published form of this article or allow others to do so, for United States Government purposes. The DOE will provide public access to these results of federally sponsored research in accordance with the DOE Public Access Plan https://www.energy.gov/downloads/doe-public-access-plan.

Appendix A. Supplementary data

The following are the Supplementary data to this article:

Supplementary material related to this article can be found online at https://doi.org/10.1016/j.mattod.2026.103187.

Data availability

Data will be made available on request.

References

[1] H. Mughrabi, Cyclic slip irreversibilities and the evolution of fatigue damage, Met. Mater. Trans. B 40 (2009) 431–453, http://dx.doi.org/10.1007/s11663-009-9240-4.

[2] J.C. Stinville, M.A. Charpagne, A. Cervellon, S. Hemery, F. Wang, P.G. Callahan, V. Valle, T.M. Pollock, On the origins of fatigue strength in crystalline metallic materials, Science 377 (6610) (2022) 1065–1071, http://dx.doi.org/10.1126/science.abn0392.

[3] H.A. Padilla, B.L. Boyce, A review of fatigue behavior in nanocrystalline metals, Exp. Mech. 50 (2010) 5–23, http://dx.doi.org/10.1007/s11340-009-9301-2.

[4] T.A. Furnish, D.C. Bufford, F. Ren, A. Mehta, K. Hattar, B.L. Boyce, Evidence that abnormal grain growth precedes fatigue crack initiation in nanocrystalline Ni-Fe, Scr. Mater. 143 (2018) 15–19, http://dx.doi.org/10.1016/j.scriptamat.2017.08.047.

[5] C. Qiu, M. Punke, Y. Tian, Y. Han, S. Wang, Y. Su, M. Salvalaglio, X. Pan, D.J. Srolovitz, J. Han, Grain boundaries are Brownian ratchets, Science 385 (6712) (2024) 980–985, http://dx.doi.org/10.1126/science.adp1516.

[6] C. Hu, D.L. Medlin, R. Dingreville, Disconnection-mediated transition in segregation structures at twin boundaries, J. Phys. Chem. Lett. 12 (29) (2021) 6875–6882, http://dx.doi.org/10.1021/acs.jpclett.1c02189.

[7] C. Hu, S. Berbenni, D.L. Medlin, R. Dingreville, Discontinuous segregation patterning across disconnections, Acta Mater. 246 (2023) 118724, http://dx.doi.org/10.1016/j.actamat.2023.118724.

[8] C. Hu, D.L. Medlin, R. Dingreville, Stability and mobility of disconnections in solute atmospheres: insights from interfacial defect diagrams, Phys. Rev. Lett. 134 (1) (2025) 016202, http://dx.doi.org/10.1103/PhysRevLett.134.016202.

[9] B.G. Clark, K. Hattar, M.T. Marshall, T. Chookajorn, B.L. Boyce, C.A. Schuh, Thermal stability comparison of nanocrystalline Fe-based binary alloy pairs, JOM 68 (2016) 1625–1633, http://dx.doi.org/10.1007/s11837-016-1868-3.

[10] H.A. Murdoch, C.A. Schuh, Stability of binary nanocrystalline alloys against grain growth and phase separation, Acta Mater. 61 (2013) 2121–2132, http://dx.doi.org/10.1007/s11837-016-1868-3.

[11] C.M. Barr, S.M. Foiles, M. Alkayyali, Y. Mahmood, P.M. Price, D.P. Adams, B.L. Boyce, F. Abdeljawad, K. Hattar, The role of grain boundary character in solute segregation and thermal stability of nanocrystalline Pt-Au, Nanoscale 13 (2021) 3552–3563, http://dx.doi.org/10.1039/D0NR07180C.

[12] P. Lu, F. Abdeljawad, M. Rodriguez, M. Chandross, D.P. Adams, B.L. Boyce, B.G. Clark, N. Argibay, On the thermal stability and grain boundary segregation in nanocrystalline PtAu alloys, Materialia 6 (2019) 100298, http://dx.doi.org/10.1016/j.mtla.2019.100298.

[13] J.F. Curry, T.F. Babuska, T.A. Furnish, P. Lu, D.P. Adams, A.B. Kustas, B.L. Nation, M.T. Dugger, M. Chandross, B.G. Clark, B.L. Boyce, C.A. Schuh, N. Argibay, Achieving ultralow wear with stable nanocrystalline metals, Adv. Mater. 30 (2018) 1802026, http://dx.doi.org/10.1002/adma.201802026.

[14] N.M. Heckman, A. Barrios, C.M. Barr, D.P. Adams, T.A. Furnish, K. Hattar, B.L. Boyce, Solute segregation improves the high-cycle fatigue resistance of nanocrystalline Pt-Au, Acta Mater. 229 (2022) 117794, http://dx.doi.org/10.1016/j.actamat.2022.117794.

[15] B. Mi, J.E. Michaels, T.E. Michaels, An ultrasonic method for dynamic monitoring of fatigue crack initiation and growth, J. Acoust. Soc. Am. 119 (1) (2006) 74–85, http://dx.doi.org/10.1121/1.2139647.

[16] E.K. Baumert, P.-O. Theillet, O.N. Pierron, Investigation of the low-cycle fatigue mechanism for micron-scale monocrystalline silicon films, Acta Mater. 58 (8) (2010) 2854–2863, http://dx.doi.org/10.1016/j.actamat.2010.01.011.

[17] A. Barrios, Y. Zhang, X. Maeder, G.M. Castelluccio, O.N. Pierron, T. Zhu, Abnormal grain growth in ultrafine grained Ni under high-cycle loading, Scr. Mater. 209 (2022) 114372, http://dx.doi.org/10.1016/j.scriptamat.2021.114372.

[18] A. Barrios, S.A. Gupta, G.M. Castelluccio, O.N. Pierron, Quantitative in situ SEM high cycle fatigue: the critical role of oxygen on nanoscale-void-controlled nucleation and propagation of small cracks in Ni microbeams, Nano Lett. 18 (4) (2018) 2595–2602, http://dx.doi.org/10.1021/acs.nanolett.8b00343.

[19] E. Hosseinian, P.-O. Theillet, O.N. Pierron, Temperature and humidity effects on the quality factor of a silicon lateral rotary micro-resonator in atmospheric air, Sensors Actuators A: Phys. 189 (2013) 380–389, http://dx.doi.org/10.1016/j.sna.2012.09.020.

[20] E.K. Baumert, O.N. Pierron, Fatigue degradation properties of LIGA Ni films using kilohertz microresonators, J. Microelectromech. Syst. 22 (1) (2013) 16–25, http://dx.doi.org/10.1109/JMEMS.2012.2212422.

[21] B.L. Boyce, H.A. Padilla, Anomalous fatigue behavior and fatigue-induced grain growth in nanocrystalline nickel alloys, Met. Mater. Trans. A 42 (2011) 1793–1804, http://dx.doi.org/10.1007/s11661-011-0708-x.

[22] C. Eberl, R. Spolenak, E. Arzt, F. Kubat, A. Leidl, W. Ruile, O. Kraft, Ultra high-cycle fatigue in pure Al thin films and line structures, Mater. Sci. Eng.: A 421 (1) (2006) 68–76, http://dx.doi.org/10.1016/j.msea.2005.10.007.

[23] H. Chen, X. Luo, M. Zhang, M. Wen, X. Zhu, G. Zhang, More severe surface relief but stronger fatigue resistance at small scales: Vacancy-assisted fatigue damage mechanism, Acta Mater. 274 (2024) 120028, http://dx.doi.org/10.1016/j.actamat.2024.120028.

[24] R.L. Fleischer, Substitutional solution hardening, Acta Metall. 11 (3) (1963) 203–209, http://dx.doi.org/10.1016/0001-6160(63)90213-X.

[25] R.L. Fleisgher, Solution hardening, Acta Metall. 9 (11) (1961) 996–1000, http://dx.doi.org/10.1016/0001-6160(61)90242-5.

[26] M. Jain, P.G. Kotula, K. Dorman, S. Desai, S. Addamane, D.P. Adams, F.W. DelRio, R. Dingreville, B.L. Boyce, Enhanced strengthening via nanoscale composition modulation, Scr. Mater. (ISSN: 1359-6462) 271 (2026) 116999, http://dx.doi.org/10.1016/j.scriptamat.2025.116999, URL https://www.sciencedirect.com/science/article/pii/S1359646225004610.

[27] F.W. DelRio, F. Mangolini, C.E. Edwards, T.F. Babuska, D.P. Adams, P. Lu, J.F. Curry, Revealing the structure-property relationships of amorphous carbon tribofilms on platinum-gold surfaces, Wear 522 (2023) 204690, http://dx.doi.org/10.1016/j.wear.2023.204690.

[28] X. Zhou, R.D. Kamachali, B.L. Boyce, B.G. Clark, D. Raabe, G.B. Thompson, Spinodal decomposition in nanocrystalline alloys, Acta Mater. 215 (2021) 117054, http://dx.doi.org/10.1016/j.actamat.2021.117054.

[29] F. Liu, R. Kirchheim, Comparison between kinetic and thermodynamic effects on grain growth, Thin Solid Films 466 (2004) 108–113, http://dx.doi.org/10.1016/j.tsf.2004.03.018.

[30] X. Song, J. Zhang, L. Li, K. Yang, G. Liu, Correlation of thermodynamics and grain growth kinetics in nanocrystalline metals, Acta Mater. 54 (2006) 5541–5550, http://dx.doi.org/10.1016/j.actamat.2006.07.040.

[31] E.A. Holm, S.M. Foiles, How grain growth stops: A mechanism for grain-growth stagnation in pure materials, Science 328 (5982) (2010) 1138–1141, http://dx.doi.org/10.1126/science.118783.

[32] C.V. Thompson, R. Carel, Stress and grain growth in thin films, J. Mech. Phys. Solids 44 (1996) 657–673, http://dx.doi.org/10.1016/0022-5096(96)00022-1.

[33] E.M. Zielinski, R.P. Vinci, J.C. Bravman, The influence of strain energy on abnormal grain growth in copper thin films, Appl. Phys. Lett. 67 (1995) 1078–1080, http://dx.doi.org/10.1063/1.114455.

[34] E.Y. Chen, P. Hamilton, B.L. Boyce, R. Dingreville, The heterogeneous nature of mechanically accelerated grain growth, J. Mater. Sci. 57 (47) (2022) 21743–21755, http://dx.doi.org/10.1007/s10853-022-07974-3.

[35] S.L. Thomas, K. Chen, J. Han, P.K. Purohit, D.J. Srolovitz, Reconciling grain growth and shear-coupled grain boundary migration, Nat. Commun. 8 (1) (2017) 1764, http://dx.doi.org/10.1038/s41467-017-01889-3.

[36] S.M. Foiles, F. Abdeljawad, A. Moore, B.L. Boyce, Fatigue-driven acceleration of abnormal grain growth in nanocrystalline wires, Modelling Simul. Mater. Sci. Eng. 27 (2019) 025008, http://dx.doi.org/10.1088/1361-651X/aaf75d.

[37] J.M. Monti, J.A. Stewart, J.O. Custer, D.P. Adams, D. Depla, R. Dingreville, Linking simulated polycrystalline thin film microstructures to physical vapor deposition conditions, Acta Mater. 245 (2023) 118581, http://dx.doi.org/10.1016/j.actamat.2022.118581.

[38] A. Stukowski, K. Albe, Extracting dislocations and non-dislocation crystal defects from atomistic simulation data, Modelling Simul. Mater. Sci. Eng. 18 (2010) 085001, http://dx.doi.org/10.1088/0965-0393/18/8/085001.

[39] A. Stukowski, V.V. Bulatov, A. Arsenlis, Automated identification and indexing of dislocations in crystal interfaces, Modelling Simul. Mater. Sci. Eng. 20 (2012) 085007, http://dx.doi.org/10.1088/0965-0393/20/8/085007.

[40] K.G.F. Janssens, D. Olmsted, E.A. Holm, S.M. Foiles, S.J. Plimpton, P.M. Derlet, Computing the mobility of grain boundaries, Nat. Mater. 5 (2006) 124–127, http://dx.doi.org/10.1038/nmat1559.

[41] J.W. Cahn, The impurity-drag effect in grain boundary motion, Acta Metall. 10 (9) (1962) 789–798, http://dx.doi.org/10.1016/0001-6160(62)90092-5.

[42] M.I. Mendelev, D.J. Srolovitz, Impurity effects on grain boundary migration, Modelling Simul. Mater. Sci. Eng. 10 (6) (2002) R79, http://dx.doi.org/10.1088/0965-0393/10/6/201.

[43] E. Nes, N. Ryum, O. Hunderi, On the Zener drag, Acta Metall. 33 (1985) 11–22, http://dx.doi.org/10.1016/0001-6160(85)90214-7.

[44] W.-B. Li, K.E. Easterling, The influence of particle shape on Zener drag, Acta Met. et Mater. 38 (1990) 1045–1052, http://dx.doi.org/10.1016/0956-7151(90)90177-I.

[45] T. Chookajorn, H.A. Murdoch, C.A. Schuh, Design of stable nanocrystalline alloys, Science 337 (2012) 951–954, http://dx.doi.org/10.1126/science.122473.

[46] C. Yang, Y. Luan, D. Li, Y. Li, N.u.H. Tariq, Very high cycle fatigue behavior of bearing steel with rare earth addition, Int. J. Fatigue 131 (2020) 105263, http://dx.doi.org/10.1016/j.ijfatigue.2019.105263.

[47] L. Li, C. Jiang, H. Wang, H. Xie, L. Li, A mechanical analysis informed fractography study on load-specific fatigue behaviors of Pt–Ir coils used in implantable medical leads, J. Mech. Behav. Biomed. Mater. 116 (2021) 104364, http://dx.doi.org/10.1016/j.jmbbm.2021.104364.

[48] K. Van Aeken, S. Mahieu, D. Depla, The metal flux from a rotating cylindrical magnetron: a Monte Carlo simulation, J. Phys. D: Appl. Phys. 41 (205307) (2008) http://dx.doi.org/10.1088/0022-3727/41/20/205307.

[49] D.P. Adams, R. Kothari, S. Addamane, J. M., K. Dorman, S. Desai, C. Sobczak, M. Kalaswad, N. Bianco, F.W. DelRio, J.O. Custer, M.A. Rodriguez, J. Boro, R. Dingreville, B.L. Boyce, Guided combinatorial synthesis and automated characterization expedites the discovery of hard, electrically conductive, Pt_xAu_{1-x} films, J. Vac. Sci. Technol. 42 (2024) 053411, http://dx.doi.org/10.1116/6.0003785.

[50] M. Rajagopalan, K. Darling, S. Turnage, R.K. Koju, B. Hornbuckle, Y. Mishin, K.N. Solanki, Microstructural evolution in a nanocrystalline Cu-Ta alloy: A combined in-situ TEM and atomistic study, Mater. Des. 113 (2016) 178–185, http://dx.doi.org/10.1016/j.matdes.2016.10.020.

[51] C.J. O'Brien, C.M. Barr, P.M. Price, K. Hattar, S.M. Foiles, Grain boundary phase transformations in PtAu and relevance to thermal stabilization of bulk nanocrystalline metals, J. Mater. Sci. 53 (2018) 2911–2927, http://dx.doi.org/10.1007/s10853-017-1706-1.

[52] N.M. Heckman, S.M. Foiles, C.J. O'Brien, M. Chandross, C.M. Barr, N. Argibay, K. Hattar, P. Lu, D.P. Adams, B.L. Boyce, New nanoscale toughening mechanisms mitigate embrittlement in binary nanocrystalline alloys, Nanoscale 10 (2018) 21231–21243, http://dx.doi.org/10.1039/C8NR06419A.

[53] T. Favaloro, J.H. Bahk, A. Shakouri, Characterization of the temperature dependence of the thermoreflectance coefficient for conductive thin films, Rev. Sci. Instrum. 86 (2) (2015) 024903, http://dx.doi.org/10.1063/1.4907354.

[54] A.P. Thompson, H.M. Aktulga, R. Berger, D.S. Bolintineanu, W.M. Brown, P.S. Crozier, P.J. in 't Veld, A. Kohlmeyer, S.G. Moore, T.D. Nguyen, R. Shan, M.J. Stevens, J. Tranchida, C. Trott, S.J. Plimpton, LAMMPS - a flexible simulation tool for particle-based materials modeling at the atomic, meso, and continuum scales, Comput. Phys. Comm. 271 (2022) 108171, http://dx.doi.org/10.1016/j.cpc.2021.108171.

[55] C. Hu, R. Dingreville, B.L. Boyce, Computational modeling of grain boundary segregation: a review, Comput. Mater. Sci. 232 (2024) 112596, http://dx.doi.org/10.1016/j.commatsci.2023.112596.

[56] D. Vizoso, M. Kosmidou, T.J. Balk, K. Hattar, C. Deo, R. Dingreville, Size-dependent radiation damage mechanisms in nanowires and nanoporous structures, Acta Mater. 215 (2021) 117018, http://dx.doi.org/10.1016/j.actamat.2021.117018.

[57] J.A. Stewart, R. Dingreville, Microstructure morphology and concentration modulation of nanocomposite thin-films during simulated physical vapor deposition, Acta Mater. 188 (2020) 181–191, http://dx.doi.org/10.1016/j.actamat.2020.02.011.

[58] K. Ahmed, C.A. Yablinsky, A. Schulte, T. Allen, A. El-Azab, Phase field modeling of the effect of porosity on grain growth kinetics in polycrystalline ceramics, Modelling Simul. Mater. Sci. Eng. 21 (2013) 065005, http://dx.doi.org/10.1088/0965-0393/21/6/065005.

[59] A. Prakash, M. Hummel, S. Schmauder, E. Bitzek, NanoSCULPT: A methodology for generating complex realistic configurations for atomistic simulations, MethodsX 3 (2016) 219–230, http://dx.doi.org/10.1016/j.mex.2016.03.002.

[60] P.M. Larsen, S. Schmidt, J. Schiøtz, Robust structural identification via polyhedral template matching, Modelling Simul. Mater. Sci. Eng. 24 (2016) 055007, http://dx.doi.org/10.1088/0965-0393/24/5/055007.